JOURNAL OF PROPULSION AND POWER
Vol. 23, No. 6, November–December 2007

Analysis of Thermal Effects in Cavitating Liquid Hydrogen Inducers

Ashvin Hosangadi,* Vineet Ahuja,† and Ronald J. Ungewitter†
Combustion Research and Flow Technology, Inc., Pipersville, Pennsylvania 18947
and
Judy Busby‡
Barber-Nichols, Inc., Arvada, Colorado 80002

DOI: 10.2514/1.28730

Evaporative cooling effects due to cavitation can significantly improve the performance of liquid rocket turbomachinery that operate with cryogenic fluids, in which the fluid is operating close to its critical temperature and the thermal effects resulting from phase change become important. A detailed numerical analysis to quantify these thermal effects of cavitation and to better understand their impact on cavitation flow physics in liquid hydrogen inducers is presented. Simulations were performed on a helical flat-plate inducer that was extensively tested in both liquid hydrogen and cold water. Predictions of cavitating performance over the operational range of inlet pressures were conducted and compared with experimental data. Fundamental differences were observed in the cavity for liquid hydrogen compared with the cold-water inducer; the cavity in liquid hydrogen shows far less vapor content, although spreading out further in the spanwise direction, which may generate blade-to-blade interactions. Thermal effects result in a more gradual breakdown of the head in liquid hydrogen resulting in improved overall performance; the liquid hydrogen inducer performed to a suction specific speed (N_{ss} number) of 75,000 and the corresponding value in water is 35,000. The temperature depressions due to evaporative cooling in the liquid hydrogen fluid are found to be only on the order of 0.5–1.0 K, highlighting the strong coupling of thermodynamic properties and the phase-change process at these flow conditions.

Nomenclature

c_m, c_g, c_L	=	speed of sound in the mixture, gas, and liquid
D_v	=	viscous flux vector
E, F, G	=	flux vectors
h_m	=	mixture enthalpy
K_f, K_b	=	rate constants for vapor and liquid formation
k, ϵ	=	turbulent kinetic energy, turbulent dissipation rate
m_t	=	rate of vapor mass formation
N_{ss}	=	suction specific speed, $\omega q^{0.5}/\text{NPSH}^{0.75}$
NPSH	=	net positive suction head, $(P_T - P_V)/\rho g$, ft
P_V	=	vapor pressure at the local fluid temperature
p	=	pressure
Q, E, S	=	vectors of conservative variables
Q_v	=	vector of primitive variables
q	=	flow rate, gpm
S	=	source term vector
T_{sat}	=	temperature saturation
u, v, w x, y, z	=	components of velocity
ΔH_v	=	latent heat formation of vapor
ρ_m, ρ_g, ρ_L	=	density of the mixture, gas, and liquid
σ_k, σ_e, C_1, C_2	=	modeling constants
$\phi_g \phi_L$	=	void fraction of the gas and liquid
Ψ_c	=	total head coefficient with cavitation
Ψ_{nc}	=	total head coefficient single phase (no cavitation)
ω	=	rotational speed, rpm

Received 6 November 2006; revision received 13 June 2007; accepted for publication 14 June 2007.

*Principal Research Scientist, 6210 Keller's Church Road. Member AIAA.
†Senior Research Scientist, 6210 Keller's Church Road. Senior. Member AIAA.
‡Project Engineer, 6325 West 55th Avenue. Member AIAA.

I. Introduction

NUMERICAL simulations of cavitating liquid rocket turbomachinery that employ cryogenic working fluids are presented in this study. Liquid rocket systems are a subset of a broader class of pumps in which the operating temperature is elevated relative to the critical temperature of the fluid and thermodynamic effects of cavitation play an important role. Typically, this results in improved mean performance of cryogenic pumps, particularly for liquid hydrogen systems. The thermal effects of cavitation were studied extensively by numerous researchers through the 1970s, including Hord [1], Stahl and Stepanoff [2], Ruggeri and Moore [3], Holl et al. [4], and Brennen [5], among others. Stahl and Stepanoff [2] were the first to estimate head depression ΔH_v values due to thermodynamic effects using the so-called B-factor method based on a quasi-static theory, in which the temperature depression was estimated in terms of the ratio of the vapor volume to liquid volume. More elaborate correlations that included dynamic effects were given later by Hord [1], Ruggeri and Moore [3], and Holl et al. [4]. The semi-empirical procedures outlined by Ruggeri and Moore [3] continue to be used currently as an engineering tool for predicting the thermodynamic depression in pumps. A more rigorous numerical procedure was developed by Cooper [6], in which a baratropic equation of state was used to define the two-phase mixture and thermal effects were evaluated with a nondimensional vaporization parameter. Most of these techniques, however, require some degree of empiricism and calibration of coefficients for specific pump geometries.

For turbomachinery simulations, the majority of cavitating-pump computational fluid dynamics (CFD) simulations presented in the literature are limited to idealized liquids (no thermodynamic effects) at design conditions. Typical simulations show comparisons with data at design conditions for the head coefficient and the critical N_{ss} number at which performance breakdown occurs (Hosangadi et al.

[7], Athavale and Singhal [8], Dupont and Okamura [9], and Medvitz et al. [10]). However, the effect of temperature variations in the fluid on the cavitating performance is, by definition, not accounted for in these calculations. A semi-analytical procedure recently developed by Watanabe et al. [11] has shown excellent comparisons of cavity length for liquid nitrogen cavities and may provide a means of predicting improvements in the performance of inducers as a function of liquid thermodynamics. A number of groups (in addition to the authors) have been working on developing compressible frameworks for cavitation problems in liquid rocket pumps, including Dorney et al. [12], Utturkar et al. [13], and Venkateswaran et al. [14] for applications in high-speed supercavitating vehicles. However, as our discussion here highlights, there is a critical need for more fundamental CFD tools that may be used to study the flowfields of cryogenic inducers.

In the present effort, a detailed numerical analysis to quantify the thermal effects of cavitation in liquid hydrogen inducers and to better understand the coupling between cavitation phase change and fluid thermodynamics is undertaken. To simulate this class of flows, a generalized compressible multiphase formulation was developed that models thermal effects of phase change and the accompanying property variations. This formulation has been validated extensively for cavitation in liquid nitrogen and hydrogen in our earlier work (Hosangadi and Ahuja [15,16]); predictions of temperature and pressure depression for flow over hydrofoils and ogives were compared with experimental data obtained by Hord [1]. The multiphase model was implemented in the CRUNCH CFD® code, which is a multi-element-based unstructured code [17] that permits a combination of hexahedral, tetrahedral, prismatic, and pyramidal elements in mesh construction. Such a framework is particularly attractive for complex turbomachine configurations such as inducers, because high-quality grids can be generated very efficiently with minimum skewness.

The liquid hydrogen inducer analyzed here has a 6-deg flat plate, helical geometry, and was extensively tested in both cold water and liquid hydrogen (Ball et al. [18], Anderson et al. [19], and Kovich [20]). We focus our attention on the design flow coefficient with the inlet temperature of liquid hydrogen at 37° R. The impact of thermal effects will be assessed by simulating the cavitating suction performance and comparing the performance at a similar flow coefficient in cold water, in which thermal effects are negligible. Additional analysis of the cavity characteristics between the liquid hydrogen and cold-water case will be conducted and, in particular, we will examine whether the cavity changes from a glassy to a frothy vapor zone in cryogenic working fluids, as has been noted in the literature [1]. For the liquid hydrogen case, the temperature depressions in hydrogen at different cavity lengths (or inlet pressures) will be quantified to identify the coupling between the thermodynamic property variations and the phase-change process. In the sections to follow, we begin with a brief description of the multiphase formulation. Simulations for the water flow tests are presented, followed by a discussion of results for corresponding simulations in liquid hydrogen. We conclude by summarizing the differences in inducer flows for the two working fluids.

II. Multiphase Equation System

The multiphase equation system is written in vector form as

$$\frac{\partial Q}{\partial t}+\frac{\partial E}{\partial x}+\frac{\partial F}{\partial y}+\frac{\partial G}{\partial z}=S+D_v \tag{1}$$

where Q is the vector of dependent variables; E, F, and G are the flux vectors; S is the source terms for the phase change; and D_v represents the viscous fluxes. The viscous fluxes are given by the standard compressible form of Navier–Stokes equations [17]. The vectors Q, E, and S are given next, with a detailed discussion on the details of the cavitation source terms to follow later:

$$Q=\begin{pmatrix}\rho_m\\ \rho_m u\\ \rho_m v\\ \rho_m w\\ \rho_g\phi_g\\ \rho_m h_m\\ \rho_m k\\ \rho_m \varepsilon\end{pmatrix}\qquad E=\begin{pmatrix}\rho_m u\\ \rho_m u^2+P\\ \rho_m uv\\ \rho_m uw\\ \rho_g\phi_g u\\ \rho_m h_m u\\ \rho_m ku\\ \rho_m \varepsilon u\end{pmatrix}\qquad S=\begin{pmatrix}0\\ 0\\ 0\\ 0\\ m_t\\ m_t h_{\mathrm{fg}}\\ S_k\\ S_\varepsilon\end{pmatrix} \tag{2}$$

The equations represented in the preceding system are in the following order in the preceding vectors: 1) mixture mass continuity, 2–4) mixture momentum (three components), 5) vapor phase mass conservation, 6) mixture energy, 7) turbulent kinetic energy and 8) turbulent dissipation rate conservation. Here, ρ_m and h_m are the mixture density and sensible enthalpy, respectively, and ϕ_g is the volume fraction or porosity of the vapor phase (note that the subscript $g$and any references to a gas imply the vapor phase and not an additional noncondensable gas component). The mixture-energy equation was formulated with the assumption that the contribution of the pressure work on the mixture energy is negligible. This is based on the premise that liquid hydrogen has minimal compressibility and that the pressure in the cavity remains close to the vapor pressure. The source term for the vapor phase arises due to cavitation, where m_t is the net rate of vapor mass generation (or condensation), and the corresponding source term for the energy equation is given as $m_t h_{\mathrm{fg}}$, where h_{fg} is the change in enthalpy resulting from the phase change and is a function of the local fluid temperature. These phase-change source terms are discussed further in Sec. III.

The mixture density, enthalpy, and vapor porosity are related by the following relations locally in a given cell volume:

$$\rho_m=\rho_g\phi_g+\rho_L\phi_L \tag{3}$$

$$\rho_m h_m=\rho_g\phi_g h_g+\rho_L\phi_L h_L \tag{4}$$

$$1=\phi_g+\phi_L \tag{5}$$

where ρ_g and r_L are the physical material densities, and h_g and h_L are the sensible enthalpy of the vapor and liquid phase, respectively, and are generally functions of both the local temperature and pressure.

Thus far, we have not made any statements defining the temperatures characterizing the liquid and vapor. In general, the liquid and vapor may not be in equilibrium locally and can have independent temperatures. Examination of temperature and pressure data for cavitation in Freon [21] reveals that the saturation vapor pressure corresponding to the local fluid temperature in fact matches the local pressure measurement. This implies that the phase-change process results in local thermodynamic equilibrium between the phases. The thermodynamic properties of the liquid and vapor in the cavity may now be defined by a single variable: the local saturation temperature T_{sat}. Hence, all thermodynamic properties (density, vapor pressure, viscosity, etc.) of both the liquid and the vapor phases may be generated as a tabular function of the saturation temperature. In our study here, these properties were generated from the standard thermodynamic database 12 available from the National Institute of Standards and Technology (NIST) for pure fluids [22]. The thermodynamic properties of the fluid were specified using the saturation values from the table corresponding to the local temperature of the fluid.

The equation system as formulated in Eq. (1) is very stiff, because the variations in density are much smaller than the corresponding changes in pressure. Therefore, to devise an efficient and accurate numerical procedure, we transform Eq. (1) to a pressure-based form in which pressure rather than density is the variable solved for. An acoustically accurate two-phase form of Eq. (1) is first derived, followed by a second step of time-scaling or preconditioning to obtain a well-conditioned system. We begin by defining the acoustic form of density differential for the individual vapor and liquid phase as follows:

$$\mathrm{d}\,\rho_g = \frac{1}{c_g^2}\,\mathrm{d}P, \qquad \mathrm{d}\rho_l = \frac{1}{c_L^2}\,\mathrm{d}P \tag{6}$$

where c_g is the isothermal speed of sound $(\partial P/\partial \rho_g)_T$ in the vapor phase, and c_L is the corresponding isothermal speed of sound in the liquid phase, which is a finite value. We note that in Eq. (6), the variation of the density with temperature was neglected in the differential form for deriving the time-marching procedure.

Following the preceding discussion, the differential form of the mixture density ρ_m using Eq. (6) is written as

$$\mathrm{d}\,\rho_m = (\rho_g - \rho_L)\,\mathrm{d}\phi_g + \frac{1}{c_\phi^2}\,\mathrm{d}P \left(\frac{1}{c_\phi^2} = \frac{\phi_g}{c_g^2} + \frac{\phi_L}{c_L^2}\right) \tag{7}$$

where c_ϕ is a variable defined for convenience and is not the acoustic speed c_m in the mixture, which will be defined later. Using Eq. (7), Eq. (1) may be rewritten as

$$\Gamma \frac{\partial Q_v}{\partial t} + \frac{\partial E}{\partial x} + \frac{\partial F}{\partial y} + \frac{\partial G}{\partial z} = S + D_v \tag{8}$$

where

$$\Gamma = \begin{pmatrix} \frac{1}{c_\phi^2} & 0 & 0 & 0 & (\rho_g - \rho_L) & 0 & 0 & 0 \\ \frac{u}{c_\phi^2} & \rho_m & 0 & 0 & (\rho_g - \rho_L)u & 0 & 0 & 0 \\ \frac{v}{c_\phi^2} & 0 & \rho_m & 0 & (\rho_g - \rho_L)v & 0 & 0 & 0 \\ \frac{w}{c_\phi^2} & 0 & 0 & \rho_m & (\rho_g - \rho_L)w & 0 & 0 & 0 \\ \frac{\phi_g}{c_g^2} & 0 & 0 & 0 & \rho_g & 0 & 0 & 0 \\ \frac{h_g\phi_g}{c_g^2} + \frac{h_L\phi_L}{c_L^2} & 0 & 0 & 0 & (\rho_g h_g - \rho_L h_L) & (\rho_g\phi_g C_{p,g} + \rho_L\phi_L C_{p,L}) & 0 & 0 \\ \frac{k}{c_\phi^2} & 0 & 0 & 0 & (\rho_g - \rho_L)k & \rho_m & 0 & 0 \\ \frac{\varepsilon}{c_\phi^2} & 0 & 0 & 0 & (\rho_g - \rho_L)\varepsilon & 0 & \rho_m & 0 \end{pmatrix} \quad \text{and} \quad Q_v = [p, u, v, w, \phi_g, T, k, \varepsilon]^T \tag{9}$$

The numerical characteristics of the Eq. (8) are studied by obtaining the eigenvalues of the matrix $[\Gamma^{-1}(\partial E/\partial Q_v)]$. The eigenvalues of the system are derived to be

$$\Lambda = (u + c_m, u - c_m, u, u, u, u, u, u) \tag{10}$$

where c_m turns out to be the well-known harmonic expression for the speed of sound in a two-phase mixture and is given as

$$\frac{1}{c_m^2} = \rho_m \left[\frac{\phi_g}{\rho_g c_g^2} + \frac{\phi_L}{\rho_L c_L^2}\right] \tag{11}$$

The behavior of the two-phase speed of sound as a function of the gas porosity indicates that at either limit, the pure single-phase acoustic speed is recovered. However, away from the single-phase limits, the acoustic speed rapidly drops below either limit value and remains at the low level in most of the mixture regime. This large variation in the speed of sound is addressed via a preconditioning procedure that is described next.

To obtain an efficient time-marching numerical scheme, preconditioning is now applied to the system in Eq. (8), to rescale the eigenvalues of the system so that the acoustic speeds are of the same order of magnitude as the local convective velocities. This is achieved by replacing Γ in Eq. (8) by Γ_p:

$$\Gamma_p \frac{\partial Q_v}{\partial t} + \frac{\partial E}{\partial x} + \frac{\partial F}{\partial y} + \frac{\partial G}{\partial z} = S + D_v$$

where

$$\Gamma_p = \begin{bmatrix} \frac{\beta}{c_\phi^2} & 0 & 0 & 0 & (\rho_g - \rho_L) & 0 & 0 & 0 \\ \frac{u\beta}{c_\phi^2} & \rho_m & 0 & 0 & (\rho_g - \rho_L)u & 0 & 0 & 0 \\ \frac{v\beta}{c_\phi^2} & 0 & \rho_m & 0 & (\rho_g - \rho_L)v & 0 & 0 & 0 \\ \frac{w\beta}{c_\phi^2} & 0 & 0 & \rho_m & (\rho_g - \rho_L)w & 0 & 0 & 0 \\ \frac{\phi_g\beta}{c_g^2} & 0 & 0 & 0 & \rho_g & 0 & 0 & 0 \\ \left(\frac{h_g\phi_g}{c_g^2} + \frac{h_L\phi_L}{c_L^2}\right)\beta & 0 & 0 & 0 & (\rho_g h_g - \rho_L h_L) & (\rho_g\phi_g C_{p,g} + \rho_L\phi_L C_{p,L}) & 0 & 0 \\ \frac{k\beta}{c_\phi^2} & 0 & 0 & 0 & (\rho_g - \rho_L)k & \rho_m & 0 & 0 \\ \frac{\varepsilon\beta}{c_\phi^2} & 0 & 0 & 0 & (\rho_g - \rho_L)\varepsilon & 0 & \rho_m & 0 \end{bmatrix} \tag{12}$$

where the parameter β was introduced to precondition the eigenvalues. The modified eigenvalues of the preconditioned system are given as

$$\Lambda_P = \left[\frac{u}{2}\left(1 + \frac{1}{\beta}\right) + c'_m, \frac{u}{2}\left(1 + \frac{1}{\beta}\right) - c'_m, u, u, u, u, u, u\right] \tag{13}$$

where

$$c'_m = \frac{1}{2}\sqrt{u^2\left(1-\frac{1}{\beta}\right)^2 + 4\frac{c_m^2}{\beta}} \tag{14}$$

Equation (14) indicates that by setting $\beta = (c_m^2/u_p^2)$, where $u_p = \max(u, 0.01\ c_m)$, the pseudo-acoustic speed is on the order of u at all mixture composition values. The well-conditioned eigenvalues provide an efficient means of converging to steady-state solutions with minimal round-off and dissipation errors in the numerical flux calculation.

III. Cavitation Source Terms

In the present effort, the cavitation source term is defined via a simplified nonequilibrium finite rate form as follows:

$$m_t = K_f \rho_L \phi_L + K_b \rho_g \phi_g \tag{15}$$

where the constant K_f is the rate constant for vapor being generated from liquid in a region in which the local pressure is less than the vapor pressure. Conversely, K_b is the rate constant for reconversion of vapor back to liquid in regions in which the pressure exceeds the vapor pressure. Here, the rate constants are specified using the form given by Merkle et al. [23]:

$$\begin{aligned}
K_b &= \begin{bmatrix} 0 & p < p_v \\ \frac{1}{\tau_b}\left(\frac{Q_\infty}{L_\infty}\right) & \left[\frac{p-p_v}{\frac{1}{2}\rho_\infty Q_\infty^2}\right] \quad p > p_v \end{bmatrix} \\
K_f &= \begin{bmatrix} 0 & p > p_v \\ \frac{1}{\tau_f}\left(\frac{Q_\infty}{L_\infty}\right) & \left[\frac{p-p_v}{\frac{1}{2}\rho_\infty Q_\infty^2}\right] \quad p < p_v \end{bmatrix} \\
p_v &= p_\infty - \frac{1}{2}\rho_\infty Q_\infty^2 * Cav\,No. \\
\tau_f &= \text{Time constant for vapor formation} \\
\tau_b &= \text{Time constant for liquid reconversion} \\
Cav.No. &= \frac{p_\infty - p_v}{\frac{1}{2}\rho_\infty Q_\infty^2}
\end{aligned} \tag{16}$$

We note that for steady attached cavitation, this simplified form may be adequate, because the cavitation time scales do not interact with the fluid time scales if the cavitation rate constants are fast enough. The sensitivity of the cavity solution to different cavitation rate constants was shown in our previous work [15]. For unsteady cavitation modeling, however, it becomes essential to integrate bubble dynamics within a dense cloud framework wherein both the number density and mean local radius of the bubbles in an evolving cloud are tracked. The development of this unsteady model for dense cloud cavitation has been developed and validated for simpler nonrotating configurations [24].

IV. Viscous Transport Properties and Turbulence Model

The laminar viscosity and thermal conductivity for each phase are obtained from the NIST-12 data bank as a function of the local fluid temperature. In flow regions in which a two-phase mixture is present, a simplified mass-weighted mixing model, consistent with the homogenous flow model assumption of Eq. (1), is assumed:

$$\mu_m^l = \mu_g^l y_g + \mu_L^l y_L, \qquad k_m^l = k_g^l y_g + k_L^l y_L \tag{17}$$

where μ_m^l and k_m^l are the laminar mixture viscosity and thermal conductivity, respectively, and y_g and y_L are the mass fractions of vapor and liquid, respectively. We note that the laminar viscosity in cryogenic fluids is substantially lower than that for water. Consequently, most cryogenic flows are characterized by high Reynolds numbers and turbulent conditions.

The effects of turbulent mixing are accounted for by employing a two-equation k-ϵ model. We are justified in using a turbulence model because we are limiting our attention to mean predictions of sheet cavitation solutions in which large-scale unsteadiness is not present in the cavity closure region. We recognize that for cloud cavitation problems, a more advanced unsteady large eddy simulation (LES) framework may be necessary. The turbulent viscosity is obtained by solving transport equations for the turbulent kinetic energy and its dissipation rate as follows:

$$\begin{aligned}
\frac{\partial \rho_m k}{\partial t} + \frac{\partial}{\partial x_i}\left[\rho_m u_i k - \left(\mu + \frac{\mu_T}{\sigma_k}\right)\frac{\partial k}{\partial x_i}\right] &= P_k - \rho_m \varepsilon + S_k \\
\frac{\partial \rho_m \varepsilon}{\partial t} + \frac{\partial}{\partial x_i}\left[\rho_m u_i \varepsilon - \left(\mu + \frac{\mu_T}{\sigma_\varepsilon}\right)\frac{\partial \varepsilon}{\partial x_i}\right] &= C_1 f_1 P_k - C_2 f_2 \rho_m \varepsilon + S_\varepsilon \\
P_k = \tau_{ij}\frac{\partial u_i}{\partial x_j}, \qquad \tau_{ij} &= -\frac{2}{3}\rho_m k + 2\mu_T * \left(S_{ij} - \frac{1}{3}\frac{\partial u_k}{\partial x_k}\delta_{ij}\right) \\
\mu_T &= C_\mu f_\mu \rho_m \frac{k^2}{\varepsilon}
\end{aligned} \tag{18}$$

where σ_k, σ_ε, C_1, and C_2 are the modeling constants, and f_1, f_2, and f_μ are empirical modeling functions to account for low Reynolds number (near the wall). (They equal unity in the high Reynolds number form.)

Low Reynolds number effects in the near wall are accounted for by using an extension of the near-wall model of So et al. [25]. This model has been shown to reproduce the near-wall asymptotic relations for the Reynolds stress and kinetic energy accurately. In this model, the damping functions f_1, f_2, and f_μ are defined as follows:

$$\begin{aligned}
f_1 &= 1.0 - \exp\left[-\left(\frac{Re_t}{40}\right)^2\right], \qquad f_2 = 1 - \frac{2}{9}\exp\left[-\left(\frac{Re_t}{6}\right)^2\right] \\
S_\varepsilon &= \frac{1}{4}c_3 \mu_L \left[\left(\frac{\partial k^{1/2}}{\partial x}\right)^2 + \left(\frac{\partial k^{1/2}}{\partial y}\right)^2 + \left(\frac{\partial k^{1/2}}{\partial z}\right)^2\right] \\
Re_t &= \frac{\rho k^2}{\mu_L \varepsilon}, \qquad f_\mu = (1 + 4Re_t^{-3/4})\tanh\left(\frac{Re_k}{125}\right)
\end{aligned} \tag{19}$$

where $Re_k = \rho\sqrt{k}y/\mu$. The constants for this model are given as follows:

$$\begin{aligned}
c_\mu = 0.09, \qquad \sigma_k = 1.4, \qquad \sigma_\varepsilon = 1.4, \qquad c_1 = 1.44 \\
c_2 = 1.92, \qquad c_3 = 2.9556
\end{aligned} \tag{20}$$

This model was tested for a number of standard turbulence test cases to verify that it gives correct boundary-layer growth and reattachment length for recirculating flows. We also applied this model to cavitation in water and obtained good results for the mean cavity length [26]. We note that the cases reported here did not exhibit large-scale unsteadiness in the cavity closure region, and our focus was on the prediction of mean cavity solutions in the absence of highly unsteady cloud cavitation in the wake. The use of a RANS methodology for the latter situation of cloud cavitation is less justifiable and more suited for a LES analysis in which the flow dynamics is not damped by large values of "turbulent" eddy viscosity. However, we do note that there are other efforts reported in the literature in which a variety of turbulence models have been evaluated for unsteady cavity simulations [27].

The net viscosity and thermal conductivity are given as the sum of the laminar and turbulent contributions:

$$\mu = \mu_m^l + \mu_T, \qquad k = k_m^l + \frac{\mu_T \cdot Cp_m}{Pr_T} \tag{21}$$

The turbulent Prandtl number was specified to be 0.9 for the calculations presented here.

Table 1 NASA inducer geometry comparison

	TN D-2553	TN D-7016 TM X-1360
Rotor tip diam., in.	4.986	4.976
Rotor hub diam., in.	2.478	2.478
Number of blades	3	3
Tip blade angle (from axial), deg	84	84
Axial length, in.	1.637	2.00
Radial tip clearance, in.	0.025	0.025
Wrap, deg	360	440
Tip thickness, in.	0.067	0.067
Hub thickness, in.	0.100	0.100

V. Simulations of the Six-Degree Helical Flat-Plate Inducer

The inducer configuration used for numerical analyses in this study is a flat-plate helical inducer that was tested at NASA John H. Glenn Research Center at Lewis Field between 1964 and 1970 ([18–20]). There were multiple tests done in different test loops and the working fluids ranged from cold and hot water to a cryogenic facility with liquid hydrogen at different inlet temperatures. For all the tests, basic performance data were taken, including head/flow non-cavitating curves and cavitating suction performance data. For some of the tests, more detailed radial profiles were measured. Three different NASA reports were used for reference: NASA TM X-1360 ([18]), NASA TN D-2553 ([19]), and NASA TN D-7016 ([20]). Although the geometry was nominally similar for these three studies in that all the inducers had a 6-deg blade angle with three blades (see Table 1), there were differences in the axial length, as well as other minor differences in the leading-edge profile. The inducer in TN D-2553 and in TM X-1360 had a sharp leading edge with a wedge shape that was symmetrical about the blade centerline (see Fig. 1). In contrast, the inducer used in TN D-7016 had the wedge offset onto the pressure surface.

A multi-element hybrid grid that models all three blades was generated to eliminate skewness in the grid at the periodic surface. Figure 2a shows details of the three-dimensional configuration and surface grid; the grid had a total of approximately 3 million cells. The general philosophy followed is to use hexahedral blocks around each blade and patch the regions between the blade blocks using tetrahedral elements. Details of the hexahedral blade blocks and the tetrahedral filler blocks are illustrated in Fig. 2b for the hub and the shroud near the leading edge. As we proceed downstream, the entire grid becomes hexahedral as the skewness reduces between adjacent blocks.

Simulation results are presented for a flow coefficient of 0.072 for a rotational speed of 14,140 rpm in water (corresponding to results in NASA TN D-7016 [20]), whereas the liquid hydrogen cases are being computed for a rotational speed of 20,000 at the same flow coefficient (corresponding to results of NASA TM X-1360 [18]).

Water calculations were also computed for the geometry in TN D-2553 (which has a shorter axial length) at the same flow conditions. Figure 3 shows the comparison of the computed total head with experimental curves from [18] (TM X-1360), [20] (TN D-7016), and [19] (TN D-2553). The computed single-phase head compares well

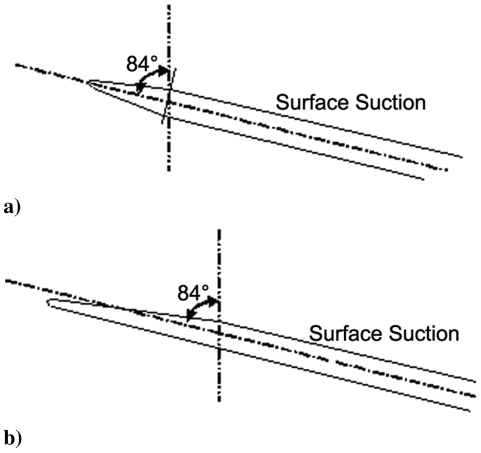

Fig. 1 Comparison of leading-edge geometry from a) TN D-2553/TM X-1360 and b) TN D-7016.

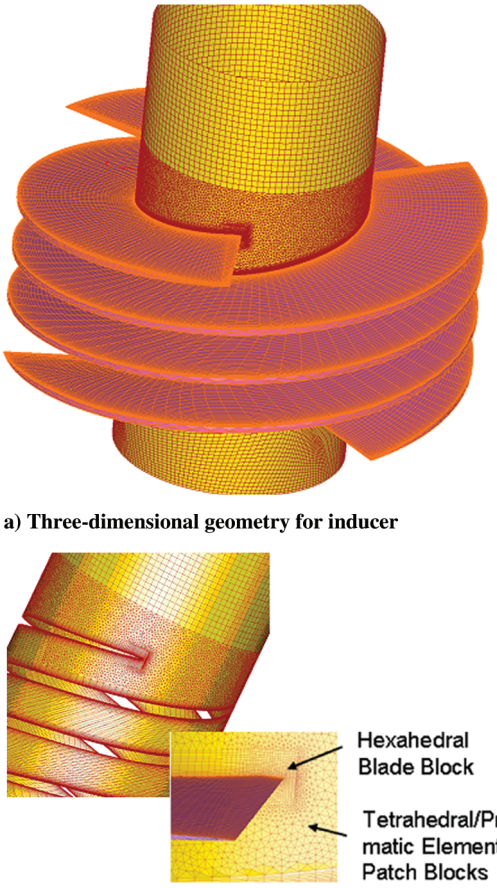

a) Three-dimensional geometry for inducer

b) Illustration of Multi-element topology on shroud and hub surface to eliminate blade-to-blade skewness

Fig. 2 Details of the numerical grid for the helical flat-plate inducer.

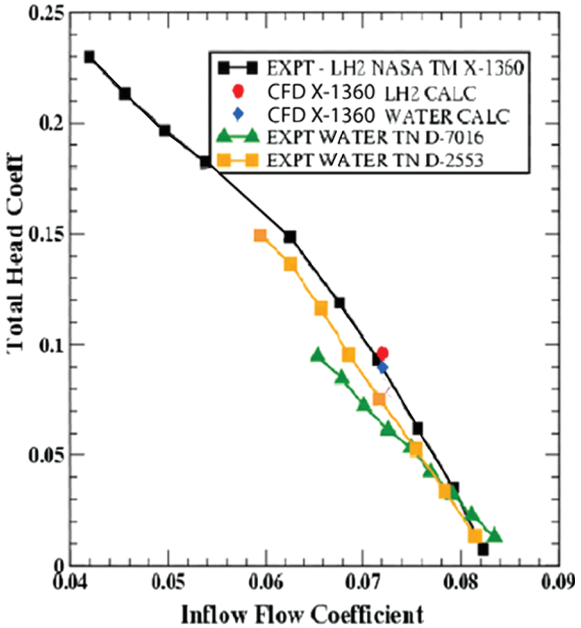

Fig. 3 Computed single-phase head coefficient at flow coefficient of 0.072 compared with experimental data.

with the respective results of TM X-1360 and TN D-2553. The computed head for liquid hydrogen is about 6% higher than that for water for identical geometries (red circle vs blue triangle); a result that is consistent with lower skin friction losses due to the much higher Reynolds number for liquid hydrogen.

The experimental results for TN D-2553 are about 20% lower than those obtained in TM X-1360 and are probably resulting from the shorter length of the inducer. The corresponding numerical simulations for this geometry (maroon diamond) come close to this lower experimental value. The only inconsistency is the difference in the experimental results for TM X-1360 and TN D-7016, which is roughly 30% lower even though the geometries are nearly identical; the authors of the report (TND-7016) did not provide any explanation for this difference.

VI. Cavitation Simulations in Cold Water

Cavitating calculations in cold water at this flow coefficient were then conducted and the inducer performance through head breakdown was simulated. Figure 4 shows contours of vapor volume fraction on the blade suction surfaces as well as the isosurface of the vapor cloud for a volume fraction of 0.4. As the suction specific speed (N_{ss} number) increases, the cavitation zone grows along the blade surface, primarily near the tip, and by an N_{ss} of 40,000, we see that the vapor front has enveloped the entire suction surface and the inducer is not generating much head.

To better understand the flow evolution, we make a cylindrical cut at a radius of 2.4 in. (close to the shroud) and unwrap the surface to better visualize the flow in the azimuthal direction. Figure 5 shows contours of vapor volume fraction at various suction specific speeds, and the corresponding pressure contours at this radius are shown in Fig. 6. In Fig. 5, we observe a slender and short cavity at an N_{ss} of 20,000 that grows substantially and comes close to the leading edge of the neighboring blade by an N_{ss} of 25,000. By an N_{ss} of 30,000, we see that the cavity is across the entire inlet of the blade passageway and generates large blockage to the oncoming flow. Head loss typically accelerates more rapidly at this point, as can be seen from the pressure contours in Fig. 6, and by an N_{ss} of 40,000, the inducer has broken down.

The cavitating performance is plotted both as a function of the N_{ss} number and of the NPSH in Fig. 7. Head breakdown begins between an N_{ss} values of 25,000 and 30,000 (NPSH between 37 and 47 ft). Comparison of the head fall-off with the experimental data of TN D-2553 and TN D-7016 indicates that the NPSH for head breakdown compares reasonably well with experimental data. However, there are qualitative differences in the head fall-off curve. The head curve for the experiments in TN D-7016 shows a gradual head drop (normalized by a single-phase value) even at large NPSH values of 80 ft, which is surprising because there should be minimal cavitation effects at this range. In contrast, the results for TN D-2553 show a much flatter head curve with much sharper and more sudden drop at breakdown. The computed results lie in between the experimental results and, at least for the purposes of comparing with the liquid hydrogen results, these comparisons are entirely reasonable.

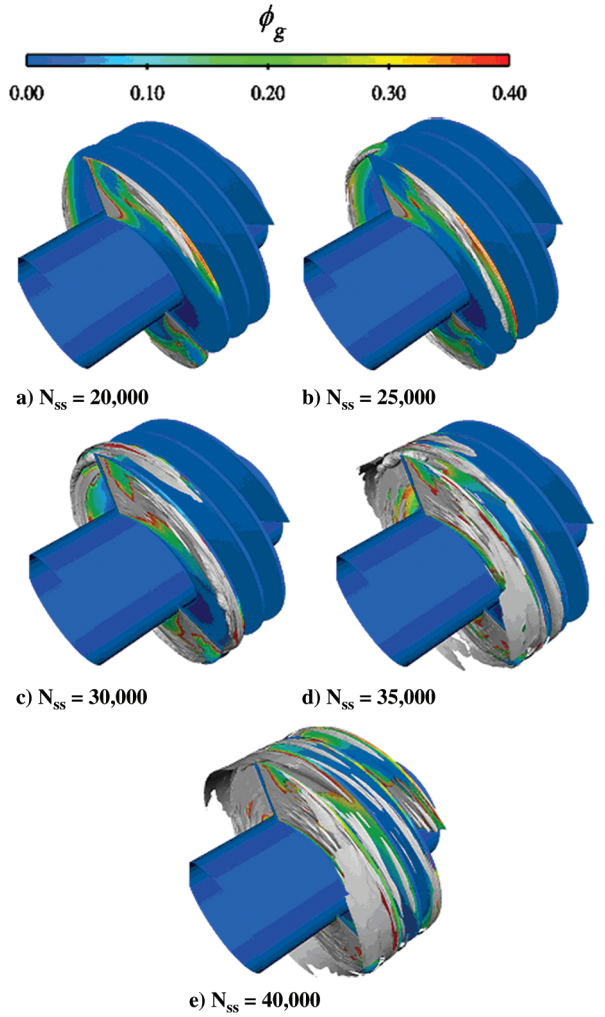

Fig. 4 Isosurface of the vapor volume fraction (at 0.4) and contours on the blade suction surface shown for various N_{ss} numbers for cold water.

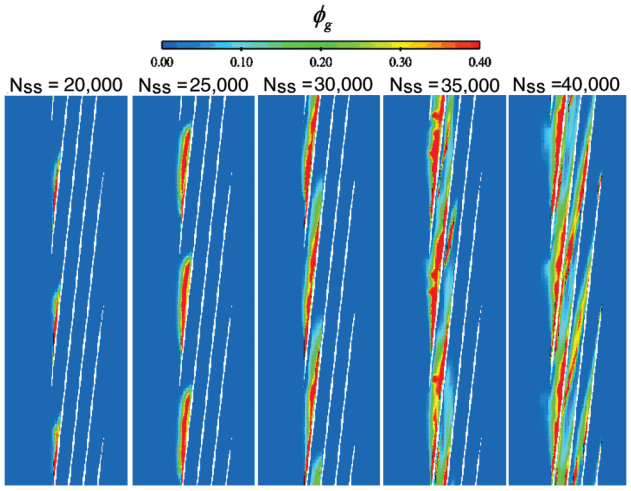

Fig. 5 Vapor volume fraction contours shown on a cylindrical cut at radius of 2.4 in. for various N_{ss} numbers for cold water.

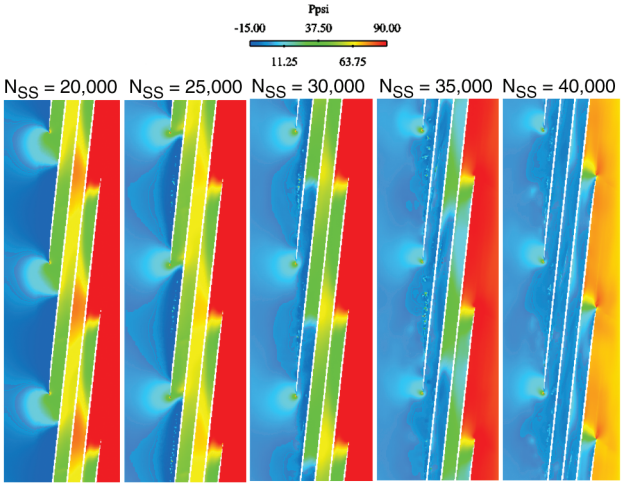

Fig. 6 Pressure contours shown on a cylindrical cut at radius of 2.4 in. for various N_{ss} numbers for cold water.

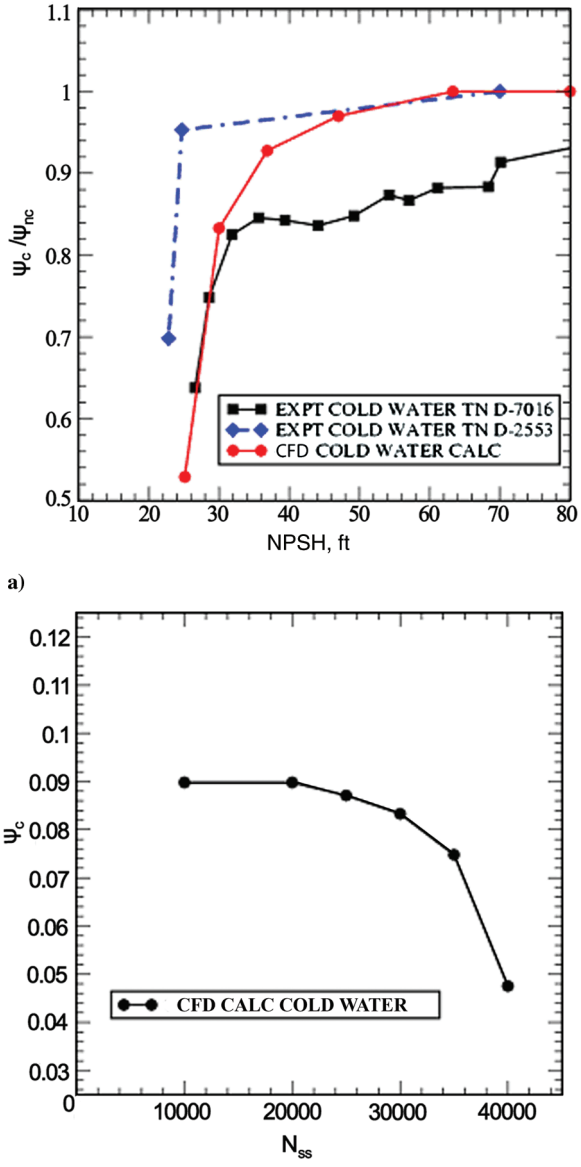

Fig. 7 Cavitating performance in cold water: a) variation with the NPSH compared with experimental data and b) variation with the N_{ss} number; CFD calculation done for geometry in TM X-1360.

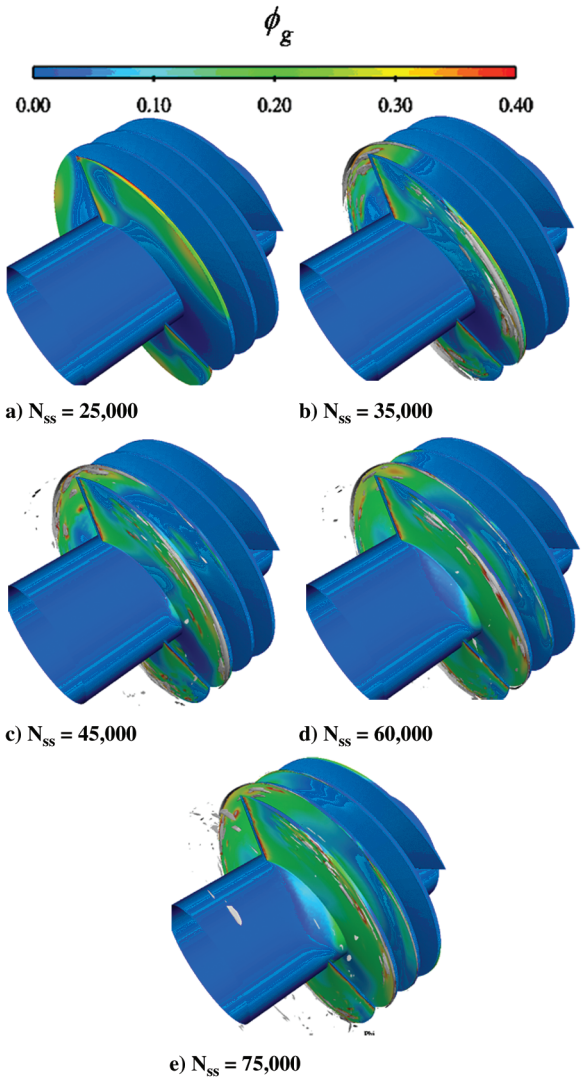

Fig. 8 Isosurface of vapor volume fraction (at 0.4) and contours on blade suction surface shown for various N_{ss} numbers in liquid hydrogen.

VII. Simulations of the Six-Degree Helical Flat-Plate Inducer in Liquid Hydrogen

Cavitating simulations of the 6-deg flat-plate inducer in liquid hydrogen for an inlet temperature of 37° R (20.55 K), a flow coefficient of 0.072, and a rotational speed of 20,000 are presented in this section. Figure 8 shows contours of vapor volume fraction, at various N_{ss} numbers, on the blade suction surfaces, as well as the *isosurface of the vapor cloud* for a volume fraction of 0.4. The equivalent figure for the cold-water calculation was shown in Fig. 4. Dramatic differences are observed between the cavitation zones in liquid hydrogen and cold water:

1) The cavity in the liquid hydrogen case is far more porous (or frothy), with significantly less vapor content.

2) The cavity is also showing increased unsteadiness at larger N_{ss} numbers, with pockets of vapor traveling upstream of the blade leading edge.

The improved performance due to thermal effects is also obvious because the inducer continues to perform at an N_{ss} number of 75,000, whereas the cold-water case had broken down completely by 40,000. These differences between water and liquid hydrogen will be analyzed in detail in the discussion to follow.

The lower vapor content and increased frothiness of the vapor cloud are apparent from the isosurface at a vapor volume fraction of 0.4. In the water case, the bulk of the vapor cloud is covered by this isosurface and hence a large portion of the cloud has at least this level of vapor content. However, for liquid hydrogen, the corresponding isosurface covers only a very small portion of the vapor cloud, indicating a much lower vapor content, leading to the frothiness (as opposed to a "glassy" water cavity) that is typically associated with cryogens. Figure 9 shows the corresponding temperature distribution on the blade surfaces. Temperature depressions of approximately 0.5 K are observed on the average, and it is the combination of the lower temperature with the lower flow blockage resulting from a higher-density vapor cloud that results in improved pump performance.

Vapor volume fraction contours at a cross-sectional radius of 2.4 in. are shown in Fig. 10. Contrasting it with the corresponding water plots (Fig. 5), we observe that the hydrogen cavity spreads out far more than the water cavity as the N_{ss} number increases. This increased spreading results in the cloud extending beyond the span of the blade passageway. In particular, at an N_{ss} number of 45,000, we observe that the cavity interacts with the leading edge of the neighboring blade and the resulting unsteadiness results in pockets of vapor being generated upstream: an effect that becomes pronounced close to breakdown ($N_{ss} = 75,000$), when the inlet pressure is already very close to the vapor pressure value. In contrast, the cavity in the water case does not spread as much and is completely enclosed within the blade passageway. Consequently, unsteady effects at the

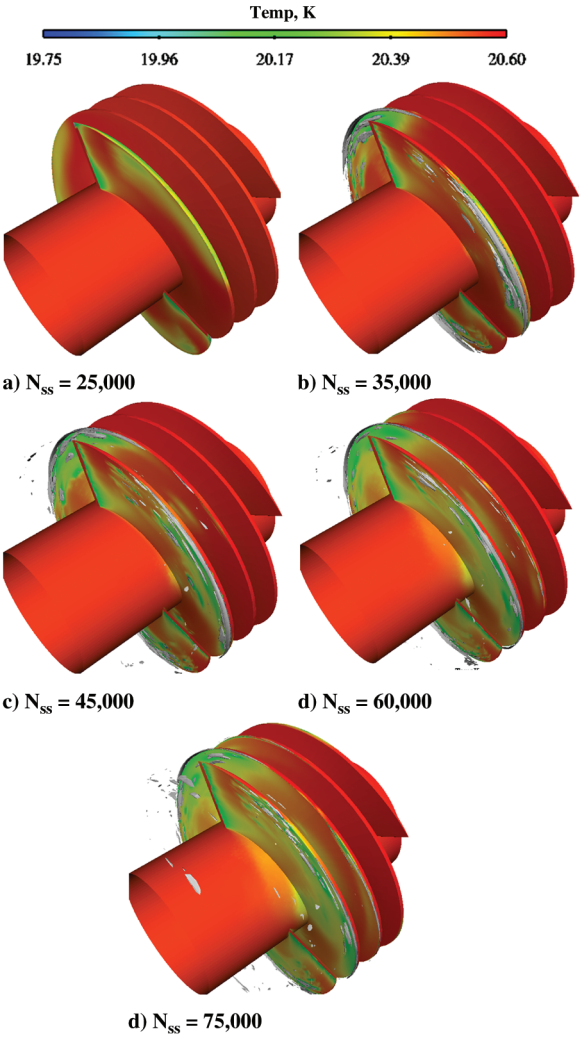

Fig. 9 Temperature contours on blade suction surface shown for various N_{ss} numbers in liquid hydrogen.

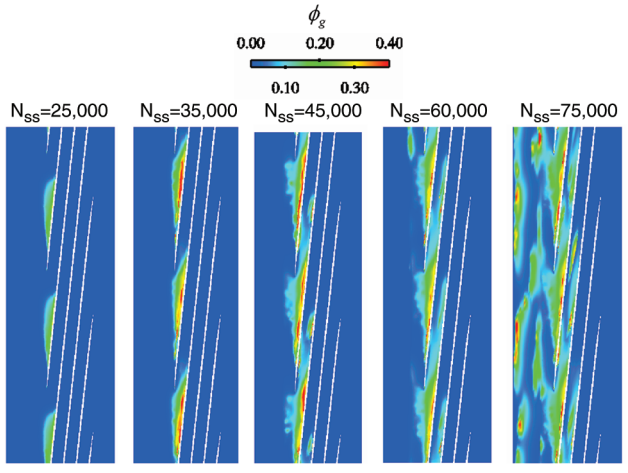

Fig. 10 Vapor contours shown on a cylindrical cut at radius of 2.4 in. for various N_{ss} numbers for liquid hydrogen.

leading edge are significantly reduced even at complete breakdown conditions.

The cavitating performance of the liquid hydrogen inducer is plotted vs NPSH in Fig. 11 and compared with experimental data at flow coefficients of 0.072, 0.074, and 0.075. We note that the geometry is identical in all of the experimental curves shown here and the numerical model matches this configuration as well: the geometry corresponds to that of TM X-1360, and the study in TN D-

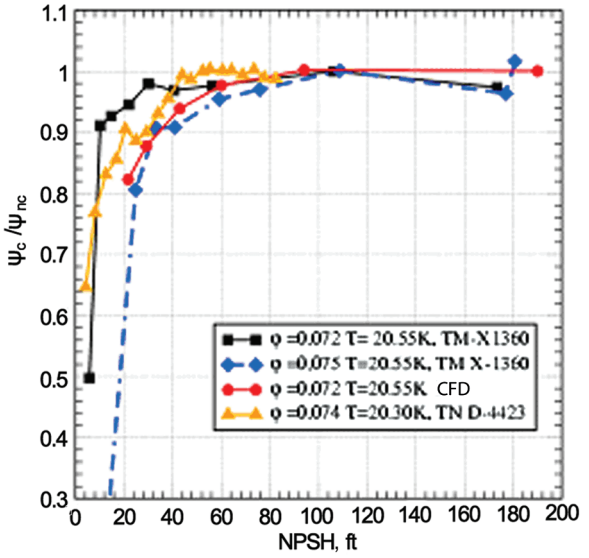

Fig. 11 Suction performance of liquid hydrogen inducer compared with cold water; CFD calculations and experiment results for geometry in TM X-1360/TN D-4423.

4423 [28] is an extension of that earlier report. The data indicate that cavitation performance for this design is sensitive to variations in flow coefficient on the order of 1.10^{-3}. It is worth noting that the system error for flow rate measurement is stated to be 16 gpm in [18] (error in the flow coefficient of 8.10^{-4}): a value that is substantial, given the sensitivity of the inducer. We also note that the report notes that some boiling may have occurred in the inlet duct at a low NPSH. This would have resulted in vapor content at the inducer inlet and potentially altered the flow coefficient further. The computed results are underpredicting the experimental results at $\Phi = 0.072$, but are close to the curve for 0.074 . This is reasonably good agreement, given the sensitivity of the inducer to small changes in flow rate. More important, the shape of the breakdown curve is also similar to the experimental data sets.

To compare the impact of thermal effects on performance, we plot the cavitating performance vs suction specific speed for liquid hydrogen and water in Fig. 12. Although the water case shows a more rapid breakdown around an N_{ss} number of 25,000, the liquid hydrogen case shows a gradual breakdown that begins around an N_{ss} number of 35,000, with the inducer close to complete breakdown at an N_{ss} of 75,000. Thus, the improvement in suction performance due

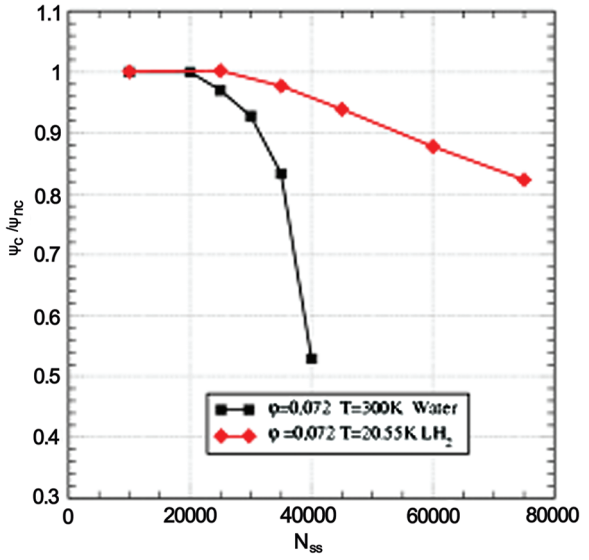

Fig. 12 Suction performance of liquid hydrogen inducer compared with cold water.

to thermal effects that suppress cavitation by lowering vapor pressure is dramatically highlighted by these results, and we note that a fundamental Navier–Stokes-based formulation is able to provide accurate simulations of the effect of fluid thermodynamics on the suction performance of complex turbomachinery systems.

VIII. Conclusions

A numerical study to quantify thermal effects of cavitation in cryogenic liquid rocket turbomachinery and to better understand the coupling between fluid thermodynamic properties and the phase-change mechanism is presented. Simulations were performed on a helical flat-plate inducer that was extensively tested in both liquid hydrogen and cold water in earlier studies by other researchers. Cavitating performance of a 6-deg flat-plate inducer with liquid hydrogen (rpm=20,000, $\Phi = 0.072$, and inlet temperature is 37°R) was simulated, and thermal effects of cavitation were deduced by direct comparison with results for cold water operating at the same flow coefficient. Excellent comparison with experimental data was noted for the cold-water calculation, with the inducer breaking down at a suction specific speed of 35,000. Cavitation performance predictions for liquid hydrogen were good, considering the complexity of the problem, and the numerical simulations showed head breakdown at a suction specific speed of 75,000, underpredicting the experimental breakdown point slightly. However, the analysis of the experimental data indicated that the head drop was extremely sensitive to both inlet temperature of the hydrogen and to the flow coefficient and that the computed head drop was very close to that obtained experimentally for a flow coefficient of 0.074 (compared with 0.072 for the calculation). The possibility of boiling in the inlet duct at high N_{ss} values was considered as a possible source of uncertainty in the data because it could alter both the inlet temperature and the flow coefficient and lead to differences with the numerical calculation.

Detailed analysis of our simulation results showed fundamental differences between the water and liquid hydrogen solutions, with the cavity in the liquid hydrogen case showing far less vapor content, although spreading out further in the spanwise direction and generating blade-to-blade interactions at larger N_{ss} numbers. Temperature depressions on the order of 0.5 K were observed in the cavity. Analysis of the flow contours taken along a cylindrical cut near the shroud indicate that head loss begins when the cavity length increases to a point at which it impacts the pressure-side profile of the neighboring blade. Further increase in the N_{ss} number results in the cavity blocking the entire blade inlet passageway, leading to substantial flow losses and accelerating breakdown.

Acknowledgments

We acknowledge funding for this work from Northrop Grumman Corporation and Barber-Nichols, Inc. under the U.S. Air Force Upper Stage Engine Technology (USET) program contract no. FA9300-04-C-0016. We would like to thank Chuck Papesh and Gordon Dressler of Northrop Grumman Corporation for the many useful discussions on this effort. We also would like to acknowledge the computer resources provided at the Naval Oceanographic Office (NAVO) Major Shared Resource Center (MSRC) site that made it possible to perform these large-scale computations efficiently.

References

[1] Hord, J., "Cavitation in Liquid Cryogens," NASA CR-2156, Jan. 1973.

[2] Stahl, H. A., and Stepanoff, A. J., "Thermodynamic Aspects of Cavitation in Centrifugal Pumps," *Journal of Basic Engineering*, Vol. 78, Nov. 1956, pp. 1691–1693.

[3] Ruggeri, S. R., and Moore, R. D., "Method for Prediction of Pump Cavitation Performance for Various Liquids, Liquid Temperature, and Rotation Speeds," NASA TND-5292, 1969.

[4] Holl, J. W., Billet, M. L., and Weir, D. S., "Thermodynamic Effects On Developed Cavitation," *Journal of Fluids Engineering*, Vol. 97, No. 4, 1975, pp. 507–516.

[5] Brennen, C. E., "The Dynamic Behavior and Compliance of a Stream of Cavitating Bubbles," *Journal of Fluids Engineering*, Vol. 95, Dec. 1973, pp. 533–542.

[6] Cooper, P., "Analysis of Single and Two-Phase Flows in Turbopump Inducers," *Journal of Engineering for Power*, Vol. 89, Oct. 1967, pp. 577–588.

[7] Hosangadi, A., Ahuja, V., and Ungewitter, R. J., "Simulations of Cavitating Flows in Turbopumps," *Journal of Propulsion and Power*, Vol. 20, No. 4, July–Aug. 2004, pp. 604–611.

[8] Athavale, M. M., and Singhal, A. K., "Numerical Analysis of Cavitating Flows in Rocket Turbopump Elements," 37th AIAA/ASME/SAE/ASEE Joint Propulsion Conference and Exhibit, Salt Lake City, UT, AIAA Paper 2001-3400, July 2001.

[9] Dupont, P., and Okamura, T., "Cavitating Flow Calculations in Industry," *International Journal of Rotating Machinery*, Vol. 9, No. 3, pp. 163–170, 2003. doi:10.1155/S1023621X03000150

[10] Medvitz, R. B., Kunz, R. F., Boger, D. A., Lindau, J. W., Yocum, A. M., and Pauley, L. L., "Performance Analysis of Cavitating Flow in Centrifugal Pumps Using Multi-Phase CFD," *Journal of Fluids Engineering*, Vol. 124, June 2002, pp. 377–383. doi:10.1115/1.1457453

[11] Watanabe, S., Hidaka, T., Horiguchi, H., Furukawa, A., and Tsujimoto, Y., "Steady Analysis of Thermodynamic Effect of Partial Cavitation Using Singularity Method," Proceedings of the 2005 ASME Fluids Meeting, American Society of Mechanical Engineers, Fluids Engineering Div. Paper 2005-77387, 2005, pp. 1–7.

[12] Dorney, D., Griffin, L., Marcu, B., and Williams, M., "Unsteady Flow Interactions Between the LH2 Feed Line and SSME LPFP Inducer," AIAA Paper 2006-5073, July 2006.

[13] Utturkar, Y., Thakur, S., and Shyy, W., "Computational Modeling of Thermodynamic Effects in Cryogenic Cavitation," 43rd AIAA Aerospace Sciences Meeting and Exhibit, Reno, NV, AIAA Paper 2005-1286, Jan. 2005.

[14] Venkateswaran, S., Lindau, J., Kunz, R., and Merkle, C. L., "Computation of Multiphase Mixture Flows with Compressibility Effects," *Journal of Computational Physics*, Vol. 180, July 2002, pp. 54–77. doi:10.1006/jcph.2002.7062

[15] Hosangadi, A., and Ahuja, V., "Numerical Study of Cavitation in Cryogenic Fluids," *Journal of Fluids Engineering*, Vol. 127, Mar. 2005, pp. 267–281. doi:10.1115/1.1883238

[16] Ahuja, V., and Hosangadi, A., "A Numerical Study in Cryogenic Fluids, Part 1: Mean Flow Parametric Studies," International Symposium on Cavitation (CAV2006), Wageningen, The Netherlands, Paper 79, 11–15 Sept. 2006.

[17] Hosangadi, A., Lee, R. A., York, B. J., Sinha, N., and Dash, S. M., "Upwind Unstructured Scheme for Three-Dimensional Combusting Flows," *Journal of Propulsion and Power*, Vol. 12, No. 3, 1996, pp. 494–503.

[18] Ball, C. L., Meng, P. R., and Reid, L., "Cavitation Performance of 84° Helical Pump Inducer operated in 37°R and 42°R Liquid Hydrogen," NASA TM X-1360, Feb. 1967.

[19] Anderson, D. A., Soltis, R. F., and Sanderock, D. M., "Performance of 84° Flat-Plate Helical Inducer and Comparison with Performance of Similar 78° and 80.6° Inducers," NASA TN D-2553, Dec. 1964.

[20] Kovich, G., "Comparison of Predicted and Experimental Cavitation Performance of 84° Helical Inducer in Water and Hydrogen," NASA TN D-7016, Dec. 1970.

[21] Ruggeri, R. S., and Moore, R. D., "Prediction of Thermodynamic Effects of Developed Cavitation Based on Liquid-Hydrogen and Freon-114 Data in Scaled Venturis," NASA TN, D-4387, 1968.

[22] "NIST Reference Fluid Thermodynamic and Transport Properties Database (REFPROP): Version 8.0," *NIST Standard Reference Database 23* [online database], http://www.nist.gov/srd/nist23.htm [retrieved 4 Sept. 2007].

[23] Merkle, C. L., Feng, J. Z., and Buelow, P. E. O., "Computational Modeling of the Dynamics of Sheet Cavitation," *Proceedings of the Third International Symposium on Cavitation (CAV98)* [CD-ROM], 1998.

[24] Hosangadi, A., and Ahuja, V., "A Numerical Study of Cavitation in Cryogenic Fluids, Part 2: New Unsteady Model for Dense Cloud Cavitation," International Symposium on Cavitation (CAV2006), Wageningen, The Netherlands, Paper No. 81, 11–15 Sept. 2006.

[25] So, R. M. C., Sarkar, A., Gerodimos, G., and Zhang, J., "A Dissipation Rate Equation for Low Reynolds Number and Near-Wall Technique," *Theoretical and Computational Fluid Dynamics*, Vol. 9, Feb. 1997, pp. 47–63. doi:10.1007/s001620050031

[26] Ahuja, V., Hosangadi, A., and Arunajatesan, S., "Simulations of Cavitating Flows Using Hybrid Unstructured Meshes," *Journal of Fluids Engineering*, Vol. 123, June 2001, pp. 331–340. doi:10.1115/1.1362671

[27] Coutier-Delgosha, O., Fortes-Patella, R., and Reboud, J. L., "Evaluation of the Turbulence Model Influence on the Numerical Simulations of Unsteady Cavitation," *Journal of Fluids Engineering*, Vol. 125, No. 1, 2003, pp. 38–45. doi:10.1115/1.1524584

[28] Meng, P. R., "Change in Inducer Net Positive Suction Head Requirement with Flow Coefficient in Low Temperature Hydrogen (27.9° to 36.6°R)," NASA TN D-4423, Mar. 1968.

T. Wang
Associate Editor